Bachelor Thesis:

Estimating the fraction of Active Galactic Nuclei hosting a black-hole binary with cosmological simulations

Peer L. Kuhlbrodt
(E-Mail: pkuhlbro@uni-muenster.de)

December 22, 2023

Contents

Estimating the fraction of Active Galactic Nuclei hosting a black-hole binary with cosmological simulations

Abstract:

Active Galactic Nuclei (AGN) play a crucial role in today's astrophysics, e.g., in the evolution of Galaxies with their central supermassive black hole. AGN are believed to be powered by a black hole (BH) accreting matter. Due to the large amount of energy that AGN can emit, they are easily observable, and a large number of AGN with measured line and continuum properties are available. Most observations of AGN are ground-based, where the resolution is approximately 1 arcsec. It is therefore not possible to differentiate if an AGN is powered by a single BH or by a black hole binary (BHB) with two BHs that have a separation of <1 arcsec. This work takes data from the IllustrisTNG hydrodynamical simulation TNG300-1 in order to estimate how many AGN of a well-known large AGN catalog could be binary systems. For this purpose, the population of potentially observable BHs in the simulation is considered, along with their sizes, luminosities, and physical distances. The fraction of binary systems in the simulation is used to make an estimation of AGN in the Rakshit catalog that host a binary system. It is found that only a small fraction of observed AGN are expected to be binary systems. The majority of those binary systems could be resolved in future space observations, that have a resolution of ~ 0.1arcsec.

1 Introduction

AGN refers to a relatively small, very bright region, which shows broad emission lines, in the center of an active Galaxy [1]. Due to the high luminosity of AGN, that can be even brighter than their host Galaxy, they are easy to observe. Due to many Surveys (e.g. [2], [3] and [4]), the number of AGN with measured spectral properties increased strongly since the discovery in 1963 by M. Schmidt [5]. Since observations (e.g. [6] and [7]) revealed that most Galaxies (if not all) host a supermassive black hole (SMBH) in their center, it is generally adopted, that AGN are powered by a SMBH accreting matter in their center [8]. Furthermore, it has been observed that AGN affect their surroundings through black hole driven feedback processes [9]. In that way, the released Energy from AGN regulate the growth and

activity of black holes and their host galaxies [10]. In addition, other investigations show, that there is a fundamental relation between SMBHs and their host Galaxies (e.g. [11] and [12]). This suggests that Galaxies evolve together with their central SMBH [10]. Therefore, AGN play a key role in understanding Galaxy formation and evolution.

This includes hierarchical growth of Galaxies through merging with other Galaxies (e.g. [13] and [1]). As a consequence, the two central SMBHs of the two merging galaxies might form a binary system (e.g. [14] and [15]). Dual AGN consisting out of two massive black holes accreting mass at subkiloparsec separations have been already observational identified (e.g. [16] and [17]). In addition, binary systems are from special interest in today's astrophysics because gravitational waves, which binary systems emit in the last stage of their evolution, became recently detectable (e.g. by the Laser Interferometer Gravitational-Wave Observatory [18]). Using pulsar time arrays (PTA) it is even possible to detect a stochastic gravitational wave background (GWB) from the superposition of many unresolved binaries (e.g. [19] and [20]).

AGN that host a binary SMBH system offer the possibility to observe and study on binary systems as they can be easily observed due to their size and brightness. While several dual AGN have been already identified, only one AGN with two black holes at pc-scale separation could be identified [21]. This work attempts to estimate the fraction of AGN hosting an unresolved binary system. These systems could be resolved in future space observation with higher resolution or through the gravitational waves they emit and could therefore give further insights in the physical processes included.

Due to improved computational power and analytic models, hydrodynamical simulations of galaxy formation and evolution became more important in today's research. Projects, such as EAGLE [22] and the Illustris simulations [23] can recreate the structures and properties of the observed universe [24]. While only limited by computational power and the respective resolution, simulations can provide insight in all physical processes. Recently adopted two modes of BH accretion in simulations [25], as it is implemented, for example, in the new generation of the Illustris model (IllustrisTNG [24]), gives rise to simulations that take kinetic AGN winds into account resulting in more realistic gas fractions, BH growth histories and thermodynamic profiles in large halos [26].

Therefore, the IllustrisTNG-model is used as a theoretical reference in this work to derive a fraction of AGN hosting an unresolved binary system, which is afterward applied to observations. The Rakshit catalog [27] containing measurements of the spectral properties of Quasars from the Sloan Digital Sky Surveys (SDSS [4]) is used as observational reference due to

the large number of cataloged AGN. Following is a brief introduction to the theoretical background of this work. In the Methods (Chapter 3) the IllustrisTNG-model and the Rakshit catalog are described in further detail. The main results of the simulation are presented and compared to the Rakshit catalog in chapter 4.1 and 4.2. Finally, a fraction of AGN hosting an unresolved binary system is derived and applied to the Rakshit sample in the conclusion (Chapter 5). Last but not least, an outlook is given in chapter 6.

2 Theoretical background

2.1 Cosmology of the universe

To describe the evolution of the universe and the formation of BHs as well as the formation of galaxies, it is mandatory to include and understand the principles of cosmology.

The standard model of cosmology is based on the cosmological principle and Einstein's theory of general relativity. The cosmological principle is the hypothesis that the universe is spatially homogeneous and isotropic on large scales [1]. According to Einstein's theory of general relativity, the structure of space-time is determined by the mass distribution of the universe [1]. Therefore, the dimensionless density parameters Ω_M and Ω_Λ, defined as

$$\Omega_M = \frac{8\pi \mathrm{G}\rho_0}{3H_0^2} \tag{1}$$

and

$$\Omega_\Lambda = \frac{\Lambda c^2}{3H_0^2} \tag{2}$$

with the mass density ρ_0, gravitational constant G and cosmological constant Λ, are dimensionless properties of the universe [28]. The subscripted 0 indicates the quantity at the current epoch, since the quantities are changing with time. The Hubble-constant at the current time H_0 is the constant of proportionality between recession speed v and distance d of the expanding universe [28].

$$H_0 = \frac{v}{d}. \tag{3}$$

As can be seen from the Hubble-constant, the universe is expanding steadily. The physical distance between two comoving observers is therefore different at different times (see section 2.2).

A third density parameter Ω_K corresponds to the curvature of space and is defined as follows [28]:

$$\Omega_K = 1 - \Omega_M - \Omega_\Lambda. \tag{4}$$

These parameters completely determine the geometry of the universe if it is homogeneous, isotropic, and matter-dominated [28].

Various observations revealed that our universe is spatially flat ($\Omega_K \approx 0$) and dominated by dark matter and dark energy. The currently used model to describe the cosmology of the universe is therefore the Λ Cold Dark Matter Model (ΛCDM-Model). It assumes that dark matter is cold and takes dark energy into account through the constant Λ, that drives the expansion of the universe. The directly observable baryonic matter makes up around 5% of the total matter in the universe. The so-described universe is consistent with most observations [29].

2.2 Redshift and scale factor

Redshift is the phenomenon by which an observer that moves relatively to a source that emits electromagnetic waves observes a shifted wavelength (Doppler effect). Quantitatively, the redshift z is defined as the fraction of shift in wavelength to emitted wavelength

$$z = \frac{\lambda_o - \lambda_e}{\lambda_e}, \tag{5}$$

where λ_o is the observed wavelength and λ_e the emitted wavelength [28].

The cosmological redshift (from now on z) is the observed shift in wavelength due to the expansion of the universe. Therefore, it is directly connected to the size of the universe. While the emitted light with wavelength λ_e travels to the observer, the universe expands and with it the wavelength. The rate at which the universe is expanding is given by the scale factor $a(t)$ which is connected to the Hubble constant $H(t)$ [1]

$$H(t) = \frac{\dot{a}(t)}{a(t)}. \tag{6}$$

Therefore, is the ratio between observed and emitted wavelengths equal to the factor by which the universe expanded in the time the light needed to the observer: [1]

$$1 + z = \frac{\lambda_0}{\lambda_e} = \frac{a(t_0)}{a(t_e)}. \tag{7}$$

Here, t_e is the time the light is emitted and t_0 the time it is observed. In Convention, the scale factor for the current time is set as $a(t_0) = 1$ [28]. This gives a direct relation between the redshift z of an observed object and the scale factor a:

$$a = \frac{1}{1 + z}. \tag{8}$$

2.3 Distances in the expanding universe

Due to the expansion of the universe, distances change with time. Therefore, cosmology distinguishes mainly between proper distance d and comoving distance d_c. Proper distance means the "actual" physical distance between objects and therefore changes with time, while comoving distance factors out the expansion of the universe, resulting in not changing with time. In convention, at redshift $z = 0$ the comoving distance is equal to the proper distance [28].

For small comoving distances δd_c the expansion of the universe gets easily factored by dividing by the scale factor a (meaning multiplying by $(1 + z)$). The total comoving distance d_C is then calculated by integrating over the infinitesimal δd_C along the radial way from $z = 0$ to the object [28].

The term $dz/E(z)$ with the function $E(z)$ defined following Peebles [30]

$$E(z) = \sqrt{\Omega_M(1+z)^3 + \Omega_K(1+z)^2 + \Omega_\Lambda}, \tag{9}$$

is proportional to the time of flight of a photon traveling the distance dz, divided by the scale factor. Due to the constant speed of light c it is a proper distance divided by the scale factor, so that the comoving distance d_c can be written as [28]

$$d_C = \frac{c}{H_0} \cdot \int_0^z \frac{1}{E(z')}\, dz'. \tag{10}$$

In a flat universe ($\Omega_K = 0$)) the comoving volume V_C within the redshift z is simply given by a sphere with the radius $d_C(z)$ [28]

$$V_C = \frac{4\pi}{3} d_C^3. \tag{11}$$

In a flat universe, the physical size s of an object at redshift z that is observed within an angle φ in radians is given by [31]

$$s = \varphi \cdot d_C(z) \cdot \frac{1}{1+z}. \tag{12}$$

2.4 Galaxy formation

The cosmological framework describes an expanding background on which the universe and its components evolve. Physical processes determine how the universe evolves from its initial conditions to the universe as it is observed today. Main processes are gravitational instability and structure formation, gas cooling, star formation, feedback processes and merger [1].

Small perturbations of the density field grow with time because regions with a slightly higher density attract their surroundings more than the average, resulting in over-dense regions becoming more over-dense and under-dense regions becoming more under-dense. This is referred to as gravitational instability [1]. Once an over-dense region exceeds a certain density, it starts to collapse due to its own gravitational pull. When an object collapses, the dark matter relaxes violently to form a dark matter halo. The gas of such an object cools and flows towards the center of the halo due to the gravitational pull. The self-gravitational pull of the gas will certainly overcome that of the halo, causing the gas to collapse and might form stars (star formation), thus giving rise to a visible galaxy in the center of the halo [1].

In the currently used ΛCDM-Model such dark matter halos hosting galaxies do not only grow through the accretion of matter from the intergalactic medium but also through merging with another halo (e.g. [32]). Consequently, dark matter halos grow hierarchically, in the sense that larger halos are formed by the coalescence (merging) of smaller progenitors [1] [13].

2.5 Black holes

Black holes (BHs) are compact objects with relatively high masses [1]. Because of their extreme gravitational potential, the space-time is deformed in such a way that nothing can escape from the event horizon of the black hole. Additionally, the extreme gravitational potential and the associated physical processes can have a significant influence on the surroundings of a BH (e.g. [33] and [9]). The numerous theoretical processes that lead to the formation of BHs are still unconstrained [34]. However, the most common theories of black hole formation are based on the collapse of stellar like objects [**?**] [35] [36].

Due to its gravitation, the BH attracts mass that falls into the BH resulting in a mass growth of the BH. This accretion of surrounding mass, mostly gas, releases energy in form of radiation. The radiation interacts with the surrounding gas, resulting in less mass falling into the BH. Assuming a spherical model, this gives a maximum luminosity, the Eddington luminosity L_{Edd}, when the pressure force on a unit volume of gas due to the scattering of photons by electrons is equal to the gravitational force of the BH. The Eddington luminosity is therefore given by

$$L_{Edd} = \frac{4\pi c G m_p}{\sigma_T} M, \tag{13}$$

with the speed of light c, the gravitational constant G, the Thomson scattering cross-section σ_T, the proton mass m_p and the mass M of the BH [1].

Assuming that the luminosity is powered by the gravitational potential, the accretion luminosity is given by

$$L = \frac{GM}{r}\dot{M}, \tag{14}$$

with the mass accretion rate $\dot{M}$, meaning the rate at which mass crosses a shell of radius r [1]. With the efficiency ϵ_r at which the rest mass of accreted material is converted into radiation,

$$\epsilon_r = \frac{L}{\dot{M}c^2}, \tag{15}$$

with the Schwarzaschild radius r_S, it follows for the Eddington accretion rate $\dot{M}_{Edd}$ [1]:

$$\dot{M}_{Edd} = \frac{L_{Edd}}{\epsilon_r c^2} = \frac{4\pi G M m_p}{\epsilon_r \sigma_T c}. \tag{16}$$

The Eddington accretion rate is the highest possible mass accretion rate for spherical mass accretion. Non-spherical accretion can reach higher mass accretion rates [1] [37].

The Bondi–Hoyle–Lyttleton accretion M_{Bondi} describes at what rate a point mass that moves through a uniform cloud of gas accretes material [38]. It is given by

$$\dot{M}_{Bondi} = \frac{4\pi G^2 M^2 \rho}{\left(c_s^2 + v_{BH}^2\right)^{3/2}}. \tag{17}$$

Here ρ and c_s are the density and speed of sound of the gas surrounding the BH and v_{BH} is the velocity of the BH. Despite the simplifications made, the Bondi–Hoyle–Lyttleton accretion made quite accurate predictions of the accretion rates of BHs [38].

In both cases of accretion, the BH is not just accreting material, but also giving constant feedback in various forms to its surrounding [1] [9]. For low accretion rates, it is believed that the feedback is mainly mechanical, e.g., jets and lobes, while for high accretion rates, it is mainly through radiative feedback [1].

2.6 Black hole binaries

BHs do not only grow in mass through accretion, as described in Section 2.5. A BH can also grow due to mergers with other BHs. This implies the formation of BH binaries (BHB) and their coalescence. From formation to coalescence, a BHB goes through different stages where different effects influence the progress until coalescence [14].

It is generally assumed that most galaxies host a BH in their center (e.g. [1] and [6]). Therefore, it is believed that after a galaxy merge, there will be two BHs orbiting in the gravitational potential of the remnant galaxy [39] [14]. At large separations $\gtrsim 1kpc$ the orbit decays due to dynamical friction until a binary forms [39] [40]. At closer separations $\lesssim 1kpc$ stellar loss cone scattering dominates the shrinking of the orbit [14]. At a separation of $\tilde{1}000$ Schwarzschild radii, the BHB starts to emit strong gravitational radiation that causes further shrinking of the orbit[14]. While these processes provide a good description of two approaching black holes until small final separations, they are not able to describe the dynamics until coalescence. This is referred to as the final-parsec problem (e.g. [41] and [42]). The timescales of the involved processes depend on the masses of the BHs, the mass of the remnant galaxy, and the surroundings of the BHB (e.g., star density and density of the surrounding gas).

2.7 Active Galactic Nuclei

Active Galactic Nucleus (AGN) refers to a small center region of an active galaxy that has a spectral energy distribution with much broader emission lines than what is expected from a collection of stars, gas and dust [1]. AGN have high luminosity that can exceed the luminosity of the host galaxy. Due to the large amount of energy that comes from a relatively small region, it is generally believed that AGN are powered by supermassive black holes (SMBH) [1] [8].

As discussed in Section 2.5 a BH can reach high luminosity through near Eddington accretion. Because of the feedback in the form of radiation, atoms in the surrounding gas of the BH get excited. The excited atoms produce strong emission lines that are typical for AGN. The gas is believed to spin in a disk toward the BH due to the gravitational potential. The broad velocity distribution around the BH due to the spinning gas causes the emission lines to be much wider than those from usual galaxies and stars. From the width of the emission lines out of the Broad Line Region (BLR), a region close to the BH ($< 0.3pc$), it is possible to determine the mass of the BH [1] [43].

2.8 Hydrodynamical simulations

All astronomical observations are limited by selection effects and the resolution of the used telescopes. For example, it is difficult to observe objects that are far away, behind other objects or have low luminosity. Therefore, it is useful to use cosmological simulations of the evolution of the universe to understand how known physical phenomena affect the formation of galaxies, stars, black holes and more. The simulations are no longer limited by observing resolution but depend on computational resolution. In general,

there are two types of simulations, zoom in simulations with higher resolution and large volume simulations with lower resolution [44]. In order to recreate a universe that is close to the observed universe, it is mandatory to implement a cosmological framework with initial conditions that are similar to the observed universe. Further on, the implemented laws of physics determine the evolution of the simulation.

As discussed in Section 2.1 the cosmological framework is believed to be described by the ΛCDM-Model. The initial conditions are by now believed to be known in high precision [44]. In order to set the initial conditions, linear perturbation theory is used to specify the perturbations on top of an expanding homogeneous background [44].

To determine the evolution of the universe, dark matter and baryonic matter must be implemented. The continuum limit of non-interacting dark matter particles is described by the collision-less Boltzmann equation coupled to Poisson's equation [44]. Because of the complexity of those coupled equations, simulations use different numerical techniques, mostly N-body methods, to solve those equations. Initially, the baryonic matter is gas, mostly hydrogen and helium. Therefore, baryonic matter is described as inviscid ideal gases following the Euler equations, complemented by various astrophysical processes [44]. Numerical techniques are also used to solve the Euler equations. The physical processes included are: gas cooling, interstellar medium, star formation, stellar feedback, SMBHs, feedback from AGN, magnetic fields, cosmic rays and radiation hydrodynamics. Many of these are implemented through effective sub-resolution models [44].

A summarized and schematic overview of the ingredients and techniques used in simulations is shown in figure 1.

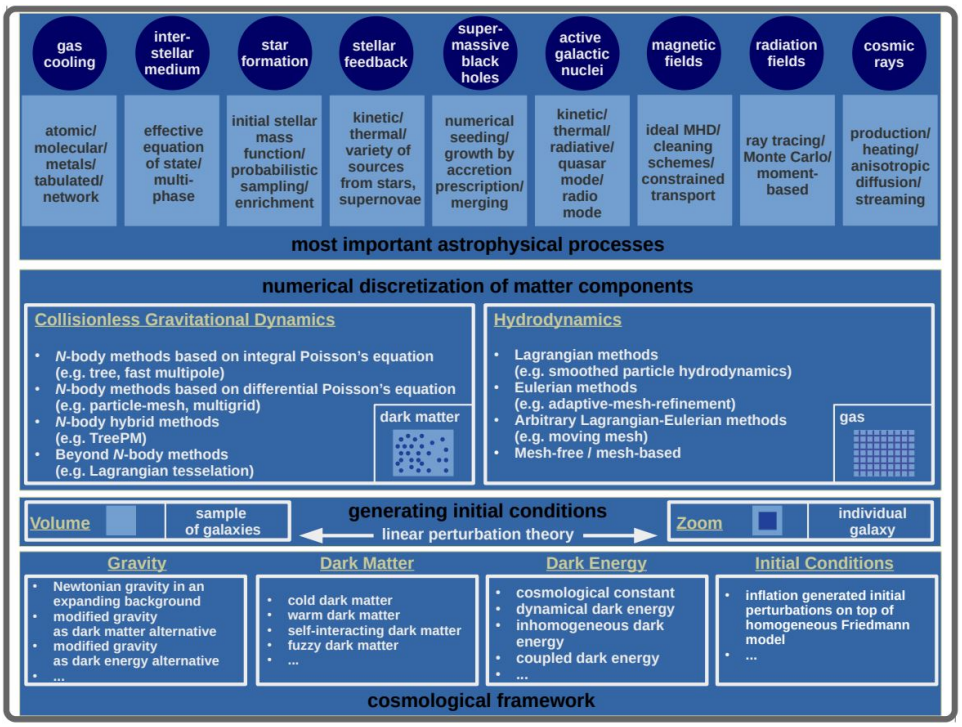

Figure 1: Schematic overview over aspects to implement Hydrodynamical Simulations of the evolution of the Universe [44].

3 Methods

Most observations of AGN are ground-based. The resolution of these observations is limited by the atmosphere to approximately $\approx$ 1arcsec. It is therefore not possible to differentiate if an AGN is powered by a single BH or by a binary system with two BHs that have a separation of < 1 arcsec. This work takes data from a hydrodynamical simulation in order to make an estimation of how many of the observed AGN are powered by a binary system.

The simulation that is looked at is the TNG300-1 run of the IllustrisTNG-model. This run was chosen due to its large volume and large number of galaxies, allowing for a statistical approach on the appearance of AGN hosting a BHB [24] [45]. Additionally, the IllustrisTNG-model implemented updated BH seeding, growth and feedback mechanisms, making it ideal to study the properties of BHs and BHBs [26]. Furthermore, IllustrisTNG provides a large, publicly accessible amount of data through screenshots at specific redshifts containing information about all particles in the simulation.

It is looked at snapshots of the simulation at different redshifts. Redshifts that are looked at are $z = 1.5$, $z = 1.0$, $z = 0.5$ and $z = 0.24$. The red-

shifts are chosen because the BH-redshift distribution peaks around $z \approx 1.5$ and because BHs at smaller redshifts are easier to observe and play a more significant role in today's research about binary systems and gravitational waves.

Due to the large number of cataloged AGN with their spectral properties and estimated BH mass, the Rakshit catalog is used as an observational reference in this work [27]. The results of the simulation are therefore compared to the Rakshit catalog in order to make a final estimation of AGN hosting a BHB in the Rakshit catalog.

In the following section 3.1 the IllustrisTNG-model is described. The Rakshit catalog is presented in Section 3.2. Further on, the data of the TNG300-1 simulation run of the model is presented and compared to the Rakshit catalog (Section 4). Finally, the estimated amount of AGN in the Rakshit catalog that are powered by a BHB is presented in the conclusion 5.

3.1 IllustrisTNG-model

The IllustrisTNG-model simulates the formation and evolution of galaxies in a large-scale cosmological, gravity+magnetohydrodynamical simulation. In the following, the implemented physics are briefly described (for further information [24] and [26] is referred).

The galaxy formation model is built upon the cosmological simulation code AREPO [24] [46]. To solve the Boltzmann equation coupled to Euler's equation, a Tree-Particle-Mesh (TPM) scheme is used. The magnetohydrodynamical equations are solved in a quasi-Lagrangian fashion. The simulation differentiates between 4 Particles: (1.) Gas, (2.) Dark Matter (DM), (2.) Stars and wind particles, as well as (4.) BHs. Astrophysical processes include star formation, stellar evolution, chemical enrichment, primordial and metal-line gas cooling, stellar feedback-driven galactic outflows, and SMBH formation, growth, and feedback. These processes are implemented in a sub-grid manner in order to have better resolution. Following the BH physics is described in more detail since this work is dealing with BHs.

A BH with seeding mass $M_{Seed} = 1 \cdot 10^6 h^{-1} M_\odot$ is seeded whenever the on-the-fly friends of friends halo finder identifies a halo with a threshold mass $M_{FOF} > 5 \cdot 10^{10} h^{-1} M_\odot$ that does not yet contain a black hole [26]. The BH gets seeded into the potential minimum of the halo. Due to numerical effects that occur when calculating gravitational forces, BHs can be displaced. To prevent this, BHs get shifted to the potential minimum of

the host halo, and its velocity is set to the mean mass-weighted velocity of the region. This has furthermore the consequence that black hole binaries promptly merge when one is found in the accretion/feedback region of the other [26].

Once seeded, a BH accretes matter with the accretion rate $\dot{M}$ set to

$$\dot{M} = \min\left(\dot{M}_{Bondi}, \dot{M}_{Edd}\right). \tag{18}$$

With the Eddington accretion $\dot{M}_{Edd}$ as defined in equation 16 with $\epsilon_r = 0.2$ and the Bondi-Hoyle-Lyttleton accretion as defined in equation 17 with $v_{BH} = 0$. The model differentiates between a high and a low accretion mode. In the high accretion mode, the BH gives feedback as pure thermal energy in a small local environment. In low accretion mode, BH-driven winds give kinetic energy to the surrounding gas, meaning the gas gets momentum but no immediate thermal energy. The kinetic feedback is more efficient than the thermal feedback. A BH is in high accretion mode as long as its fraction $\dot{M}_{Bondi}/\dot{M}_{Edd}$ exceeds the threshold χ that is given by

$$\frac{\dot{M}_{Bondi}}{\dot{M}_{Edd}} \geq \chi = \min\left[\chi_0 \left(\frac{M}{10^8 M_\odot}\right)^\beta, 0.1\right]. \tag{19}$$

With the parameters $\chi_0 = 0.002$ and $\beta = 2$ [24].

The IllustrisTNG-model provides various properties of all BHs at 100 different snapshots through the whole simulation run. The properties mainly used in this work are mass M, mass accretion rate $\dot{M}$, estimated Eddington accretion rate $\dot{M}_{Edd}$, the coordinates and the density ρ.

3.2 Rakshit catalog

The Rakshit catalog contains measurements of the spectral properties of a total of 526,265 quasars, selected from the fourteenth data release of the Sloan Digital Sky Survey (SDSS-DR14) covering $9376 deg^2$ of the hemisphere[27]. Quasars form the most luminous class of AGN and their spectra have non-thermal continua and contain strong and broad high excitation emission lines [1]. The quasars were selected based on i-band absolute magnitude $M_i(z = 2) < -20.5$ and having at least one emission line with a full width at half maximum (FWHM) larger than 500km/s or having interesting or complex absorption features [27].

From the luminosity at certain wavelengths, the bolometric luminosity is derived using the bolometric correction factor [27]. From the continuum and line properties of several emission lines, namely Hβ, Mg II and C IV,

the single-epoch virial black hole masses are derived. Quality flags are used to qualify the derived quantities. Here, Quality flags are integer numbers calculated as $2^{Bit_0} + 2^{Bit_1} + 2^{Bit_2} + ... + 2^{Bit_n}$. Further criteria are used to assign the values 0 (no flag raised) or 1 (flag raised) to each Bit (criteria can be seen in appendix A). Therefore, a quality flag = 0 indicates that no flags were raised, and thus the corresponding quantity is reliable. To keep uncertainties small, this work only considers AGN of the Rakshit sample with a signal-to-noise ratio > 3/pixel and mass and bolometric luminosity flag = 0.

This leaves a total of 298, 278 Quasars, covering a wide range of redshift between 0.038 and 5.033 and black hole masses ($\log M_{BH}$; $M_\odot$) between 6 and 11. Furthermore, the sample covers a range of bolometric luminosity ($\log L_{bol}$; erg/s) between 44.4 and 47.3. In Figure 2 the redshift distribution and mass to bolometric luminosity distribution of the Rakshit sample can be seen, colour-coded by redshift z.

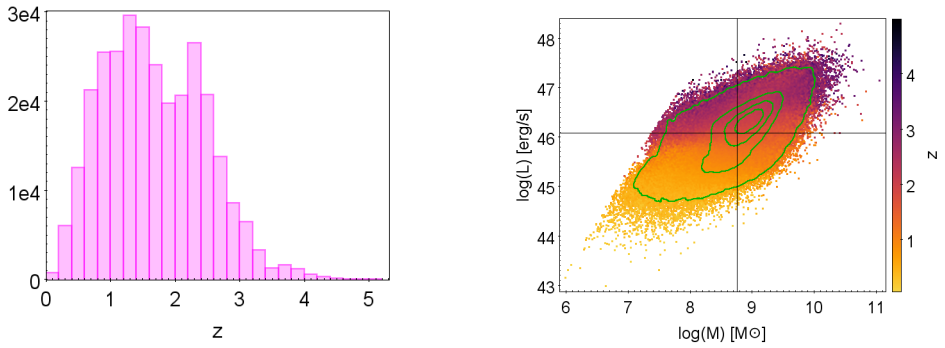

Figure 2: Left: The redshift z distribution of the Rakshit sample. Right: The mass to bolometric luminosity distribution of the Rakshit sample, color-coded by redshift z. The black lines show the mean mass and mean bolometric luminosity of the sample. The green density lines include 99; 88; 77 and 65 % of the sample. Included are only sources with a signal-to-noise ratio > 3/pixel and quality flag = 0 for the mass and bolometric luminosity estimation.

4 Analysis

The approach of this work is to compare the results of the TNG300-1 simulation run of the IllustrisTNG-model with observations, namely the Rakshit catalog, to conclude on the statistical occurance of AGN hosting a BHB. In this process, it needs to be considered that the simulation as well as the catalog work upon the ΛCDM-model with different cosmological parameters. In table 1 the cosmological parameters of the simulation and catalog are shown.

	TNG	Rakshit
H_0	67.74	70
Ω_M	0.3089	0.3
Ω_Λ	0.6911	0.7

Table 1: Cosmological Parameters used in the simulation (TNG) and the Rakshit sample.

Simulation and observations assume a flat universe with slightly different proportions of matter and a slightly different Hubble constant H_0. Since the simulation tries to recreate the observed universe, the cosmological frameworks of the simulation and observations are in sufficient agreement. Following the BH population of the TNG300-1 run at different redshifts is presented. Afterwards the BH population is compared to the AGN population of observations.

4.1 Results of the IllustrisTNG simulation

4.1.1 Black hole mass distribution

The TNG300-1 simulation run of the IllustrisTNG-model produces BH mass distributions at different redshifts, as shown in figure 3.

The lowest mass is $10^6 M_\odot$ since it is the seeding mass. For all redshifts most of the BHs in the simulation are "new" black holes, meaning they are freshly seeded, have masses of $log(M) < 7.1$ and did not have enough time to grow through mass accretion or mergers to reach higher masses (grey in the figure). The formation and early growth of BHs are observationally as well as theoretically poorly understood (e.g. [47]) and highly simplified in the simulation [26]. To reduce the impact of the simplified seeding process, a mass cut of $log(M) > 7.1$ is applied (pink in the figure). In addition, the mass cut is in good agreement with observations because most detected AGN have masses above $10^{7.1} M_\odot$.

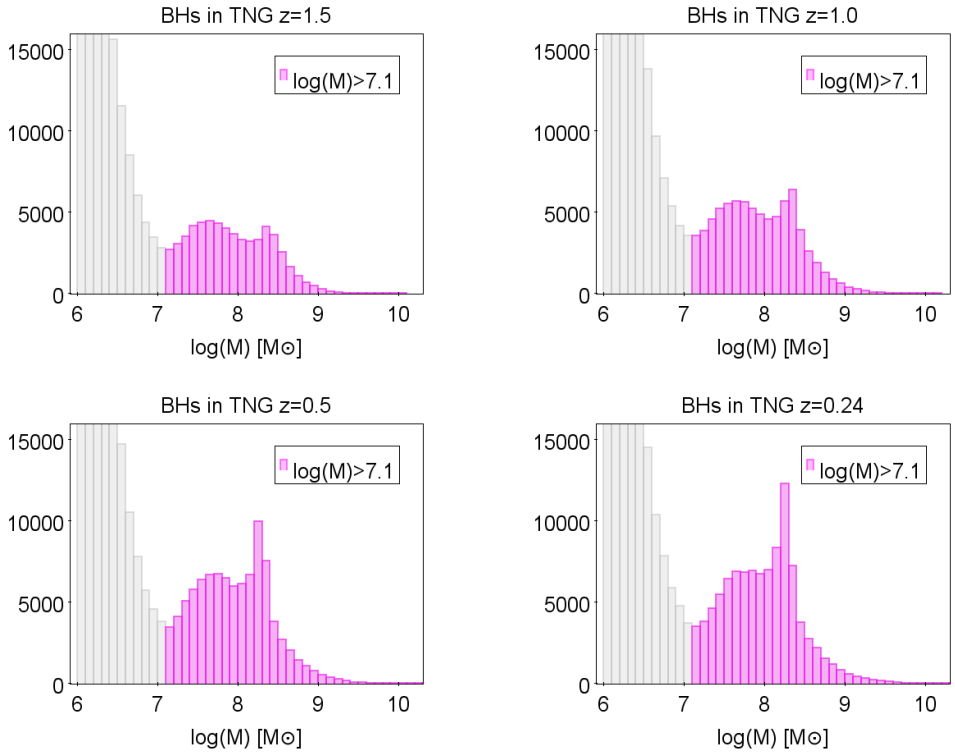

Figure 3: The logarithmic mass distribution of the TNG300-1 run at redshifts $z = 1.5$ (upper left), $z = 1.0$ (upper right), $z = 0.5$ (down left) and $z = 0.24$ (down right). A mass cut at $10^{7.1} M_{\odot}$ is visualized in pink.

The total population of BHs increases with time due to new BHs that get seeded. Because of mass accretion and mergers, the mass distribution shows more massive black holes at lower redshifts. It can also be seen that a second peak of the mass distribution is emerging at $\sim 10^{8.2} M_{\odot}$ which increases with time. This peak appears because massive BHs tend to switch in this mass range to the low accretion mode, resulting in a low accretion rate. Therefore, over time, BHs accumulate in this mass range. More about how the accretion modes affect the BH population in the simulation is in the next section 4.1.2.

4.1.2 Accretion mode

The accretion rate and mode of the BHs in the simulation are of significant importance since it is generally believed that the luminosity of BHs is powered by the accretion of mass, and the accretion mode has a direct influence on the BH's surroundings through the implemented feedback. The Eddington ratio R_{Edd} to mass is plotted in Figure 4. The Eddington ratio

is defined as

$$R_{Edd} = \frac{\dot{M}}{\dot{M}_{Edd}} = \begin{cases} 1 & \text{if } \dot{M}_{Bondi} > \dot{M}_{Edd} \\ \frac{G\varepsilon_r \sigma_T c}{m_P} \cdot \frac{\rho M}{c_s^3} & \text{if } \dot{M}_{Bondi} \leq \dot{M}_{Edd} \end{cases} \tag{20}$$

With the Eddington accretion rate and Bondi-Hoyle-Little accretion rate defined in equation 16 and 17. How the two different kinds of feedback influence the density ρ around the BH is shown as well. For better overview and understanding, the mass cut is not applied. BHs that have an Eddington ratio above the threshold χ (black line) are in high accretion mode.

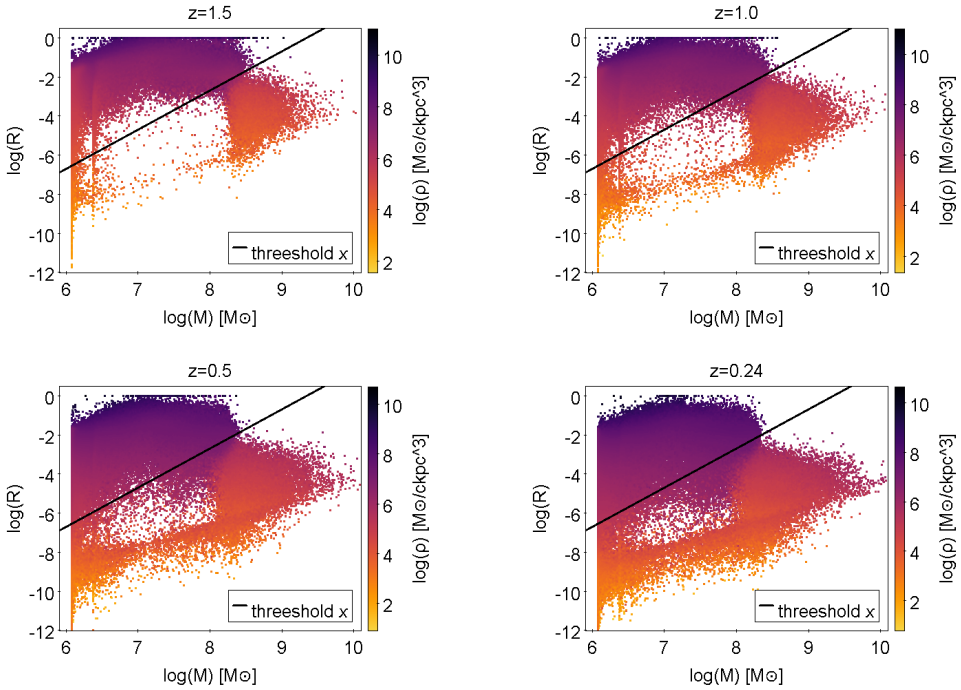

Figure 4: Mass to Eddington ratio R_{Edd} of the BHs in the simulation at redshifts of 1.5 (upper left), 1.0 (upper right), 0.5 (down left), and 0.24 (down right). In color, the comoving gas density averaged over the nearest neighbors of the BH can be seen. The black line represents the threshold χ. BHs with an Eddington ratio above χ are in high accretion mode.

Especially at redshift $z = 1.5$ the effect of the two accretion modes is visible (see figure 4. Two groupings of BHs form: a group with low masses and high Eddington ratios, as well as a group with higher masses and lower Eddington ratios. This originates from the threshold that defines in which accretion mode a BH is (equation 19). Thus, BHs with low masses are in high accretion mode and accrete close to the Eddington rate. Because the simulation limits the accretion ratio to the Eddington accretion rate, several

BHs with $R_{Edd} = 1$ appear. Since the threshold scales with $\chi \propto M^2$, BHs with higher masses switch to the low accretion mode with more efficient feedback. As a consequence, the density and therefore also the Eddington ratio ($R_{Edd} \propto M \cdot \rho / c_s^3$) drops significantly, making it likely to stay in the low accretion mode.

With lower redshift, a third group of BHs with low masses and low Eddington ratios becomes more recognizable. These BHs are already seeding in low accretion mode and accreting over the hole simulation with low accretion rates. This occurs because the density of the surrounding gas around those BHs is so low that it prevents high accretion rates. In general, at lower redshifts, it becomes noticeable that the Eddington accretion ratio scales also with the density $R_{Edd} \propto M \cdot \rho / c_s^3$ of the surrounding gas. At those redshifts, BHs had enough time to accrete gas until the gas reservoir itself lowered the Eddington ratio, resulting in the groups becoming blurry along the y axes.

4.1.3 Black hole feedback region

In the high accretion mode, feedback is given to a small local environment, while in the low accretion mode, feedback is given more widely through BH-driven winds. The accretion mode of a BH has therefore a direct influence on the size of the feedback region. The size of the feedback region of a BH is here defined by the comoving radius r_C of the sphere enclosing the 64 nearest-neighbor gas cells. Other simulations with higher resolution can have a much wider definition of the feedback region (e. g. 256 for zoom in simulations [26]), but due to the large scale of the TNG300-1 run and limited computing power, the neighborhood of a BH is here set to the 64 nearest-neighbor gas cells [26]. The distribution of r_C can be seen in figure 5.

As expected from the implemented feedback modes, the size of the feedback region depends mainly on the accretion mode of the BH. In this context, have BHs in high accretion mode significantly smaller feedback regions than BHs in low accretion mode (see figure 5).

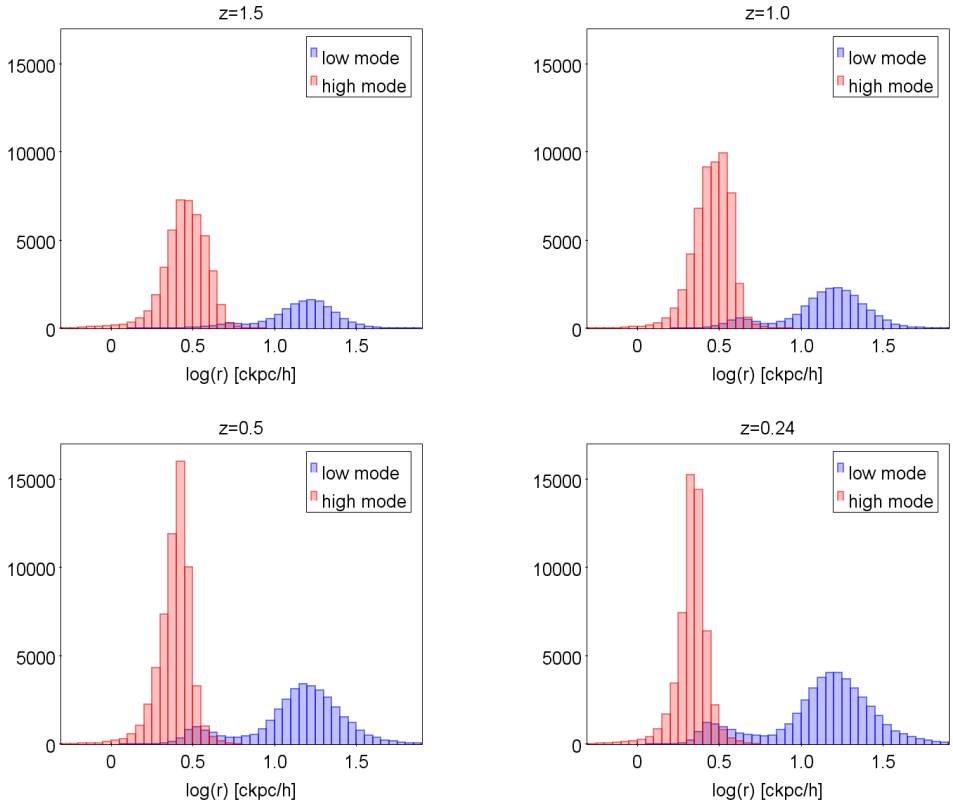

Figure 5: Distribution of the comoving radius r_C of the sphere enclosing the 64 nearest-neighbor gas cells of a BH at redshifts 1.5 (upper left), 1.0 (upper right), 0.5 (down left), and 0.24 (down right). This defines the size of the feedback region from a BH. Distributions are shown for BHs in low accretion mode (blue) and high accretion mode (red).

4.1.4 Black hole binary resolution

Two BHs in the simulation promptly merge if one is found in the feedback region of the other. This means two BHs that have a smaller separation than the comoving radius r_C of one of the BHs are merged by the simulation and will appear as a single remnant BH in the next time step. Therefore, BHBs with small separations $< r_C$ are not resolved by the simulation.

The logarithmic distributions of the comoving radii were fit with a Gaussian curve to determine the mean comoving radii $\bar{r}_C$ for BHs in high and low accretion modes. The maximum observable separation of ground-based observations s_{max} within 1arcsec at a given redshift z is given by equation 12. The maximum observable separation and mean comoving radii $\bar{r}_C$ for each snapshot can be seen in table 2.

z	low mode $\bar{r}_{C,low}$ [ckpc/h]	high mode $\bar{r}_{C,high}$ [ckpc/h]	s_{max} [ckpc/h]
1.5	14.191	2.807	14.71
1.0	13.642	2.834	11.153
0.5	13.598	2.451	6.389
0.24	13.404	2.151	3.29

Table 2: The mean comoving radii $\bar{r}_C$ derived from a Gaussian fit of the comoving radius distribution and the maximum observable separation s_{max} as it would be resolved in ground-based observations for each snapshot of the simulation. The mean comoving radius corresponds to the mean distance at which two BHs in each mode will be merged by the simulation.

When concluding from the simulation on the statistical occurrence of BHBs that would appear unresolved in observations (meaning they have separations of $< s_{max}$, as adequate for a ground-based observation, limited to $\sim$ 1arcsec in resolution), it needs to be considered that the simulation already promptly merged BHBs at that scale. Using the BHB fraction based on the simulation to estimate how many observed AGN host a binary system gives therefore just a lower limit because the observed sample might contain binary systems with close separations $< \bar{r}_C$ as they are not resolved in the simulation.

4.1.5 Black hole binaries

The aim of this work is to estimate how many observed AGN host an unresolved BHB. In order to be able to assume that a BHB would be unresolved in ground-based observations, its BHs need to have a smaller separation than 1arcsec or s_{max} (see table 2). The IllustrisTNG-Model provides the coordinates of all BHs in the simulation. The coordinates were used to identify all BHBs that would appear unresolved with ground-based observations (from now on meant by uBHB). The numbers of observable BHs (oBH) and uBHBs in the simulation can be seen in table 3. oBH counts all objects that would be observed as one BH in ground-based observations, meaning a uBHB is counted as one individual oBH.

Having found all uBHBs in the simulation it needs to be determined which properties would be observed. Looking at an unresolved BHB the mass would be estimated from the overlaid emission lines of the two BHs. The overlaid emission lines are thereby dominated by the brighter BH; hence, the mass of a uBHB would be observed as the mass of the brighter BH.

The luminosity of a BH comes from a region that is $\sim$ 0.3 pc in size.

z	# oBH	# uBHB	Fraction of uBHBs [‰]
1.5	58822	38	0.646
1.0	77717	15	0.193
0.5	94595	10	0.106
0.24	100387	7	0.070

Table 3: Number of oBHs and uBHBs in the simulation. uBHB coresponds to a binary system at a separation of $<$ 1arsec. The number of oBHs is the sum of all single BHs and uBHBs in the simulation. The fraction of uBHB is $\#oBH/\#uBHB$.

Therefore, it is assumed when looking at a uBHB that the light-emitting regions do not overlap. Thus, the observed total luminosity L_{tot} of a uBHB is assumed to be the sum of the individual luminosity L_1 and L_2 of the two BHs:

$$L_{tot} = L_1 + L_2. \tag{21}$$

The luminosity of a BH in the simulation is defined in chapter 4.2.2.

In summary, a uBHB in the simulation is a binary system at a separation of $<$ 1arcsec and would be observed in ground-based observations as an individual BH with the mass of the brighter BH and the luminosity L_{tot}.

4.2 Comparison to the Rakshit catalog

In this section, the BH population of the simulation is compared to the observed AGN population of the Rakshit catalog in order to examine the ability of the simulation to recreate a BH population as observed. In this context, it needs to be considered that simulation and observations investigate different volumes (see 4.2.1).

As seen above, the simulation produces a BH population with broad distributions of masses and accretion rates. Only a small fraction are uBHBs. The Rakshit sample, on the other hand, contains only a selection of sources that have been classified as AGN because of their high luminosity and broad emission lines. Therefore, it is useful to use the bolometric luminosity as a comparative criterion because a high luminosity is, beside broad emission lines, the main selection criteria of the Rakshit sample. The populations of simulation and observations are compared in their bolometric luminosity and masses in section 4.2.2.

4.2.1 Volume comparison

The simulation takes snapshots at exact redshifts, where all quantities of all BHs are determined at one exact redshift, while the observations do not observe BHs at one exact redshift. To compare the single redshift properties to observations, it is mandatory to consider BHs that were observed in a redshift interval. The observed comoving Volume is thereby defined by the redshift interval $z_1 < z_2$ as

$$V_{z_1,z_2} = V_{C,z_2} - V_{C,z_1}. \tag{22}$$

With the comoving volume V_C within the redshift z given by equation 11. Since the surveys of the Rakshit Catalog cover $9376 deg^2$ of the hemisphere, the observed volume V_{Rak} of the Rakshit Catalog in a redshift interval is given by

$$V_{Rak} = V_{z_1,z_2} \cdot \frac{9376}{41253}. \tag{23}$$

The comoving volume of the simulation is given by

$$V_{TNG} = \left(L\frac{1}{h}\right)^3 \approx 0.027716\text{Gpc}^3, \tag{24}$$

with the side length $L = 205$Mpc of the simulation [48].

In table 4 the redshift of the considered snapshots and the corresponding redshift interval of the Rakshit catalog, as well as the observed volume, can be seen. Added are also the amount of BHs in the simulation, the amount of AGNs in the Rakshit sample, and the scalingfactor $\alpha = V_{Rak}/V_{TNG}$.

TNG		Rakshit			
z	# BH	z	$V_{Rak}[\text{Gpc}^3]$	# AGN	α
1.5	58822	$1.4 - 1.6$	20.0423	28251	723.1300
1.0	77717	$0.9 - 1.1$	15.1351	23822	546.0766
0.5	94595	$0.4 - 0.6$	6.6689	12517	240.6142
0.24	100387	$0.14 - 0.34$	2.1030	3878	75.8777

Table 4: The redshift and amount of BHs for each snapshot of the simulation (TNG) is shown. The corresponding redshift interval, volume and amount of observed AGN of the Rakshit sample can be seen as well. Also added is the scalingfactor α, which can be used to scale the simulation to the volume of the observations.

When comparing the simulation to observations, it needs to be considered that the comoving volume of the simulation is smaller than the observed volume. In addition, the comoving volume of the simulation stays the same

while the observed volume shrinks with lower redshifts. The effect of the volume on the BH and AGN populations can be factored out with the scalingfactor α.

4.2.2 Mass and bolometric luminosity comparison

The AGN of the Rakshit sample are observed through their radiation. Out of the spectrum and emission lines, their bolometric luminosity and masses are derived. The simulation does not provide any spectra, luminosity, or emission lines but directly calculates properties such as mass, accretion rate and density around the BH. Nevertheless, the bolometric luminosity of a BH in the simulation can be estimated following equation 15 by

$$L_{TNG} = c^2 \epsilon_r \dot{M}. \tag{25}$$

The efficiency ϵ_r at which the rest mass of accreted material is converted into radiation is in the IllustrisTNG-model set to $\epsilon_r = 0.2$ [26].

In figure 6 the mass to bolometric luminosity distribution of the simulation and Rakshit sample can be seen. The appearance of the mass to bolometric luminosity distribution of the simulation is described in further detail in section 4.1.2.

It can be seen in figure 6 that the two populations of simulation and observations overlap only at high bolometric luminosity. This occurs because the Rakshit sample selects AGN of high luminosity that have broad emission lines, and is therefore strongly incomplete at low luminosity. Furthermore, light and less luminous AGN are more difficult to detect, especially at higher redshifts. At lower redshifts these AGN can be detected, but the observed volume is smaller, and therefore it is unlikely to find the most massive and luminous AGN. That is why the distribution of the Rakshit sample shifts from the most massive and luminous AGN at high redshift to lighter, less luminous AGN at lower redshifts. In addition, the simulation limits the accretion rate to the Eddington accretion rate (the line of the most luminous BHs, Eddington luminosity, of the simulation in figure 6) while the Rakshit sample contains BHs with higher accretion rates.

The goal is to derive a mass and bolometric luminosity range $]M_{min}, M_{max}[$ and $]L_{min}, L_{max}[$ in which the two populations match sufficiently well in order to apply the uBHB fraction of the simulation to the observed sample. The matching bolometric luminosity range is here limited on the one side by the Rakshit sample and on the other side by the simulation, which is limited to Eddington luminosity. The matching bolometric luminosity range

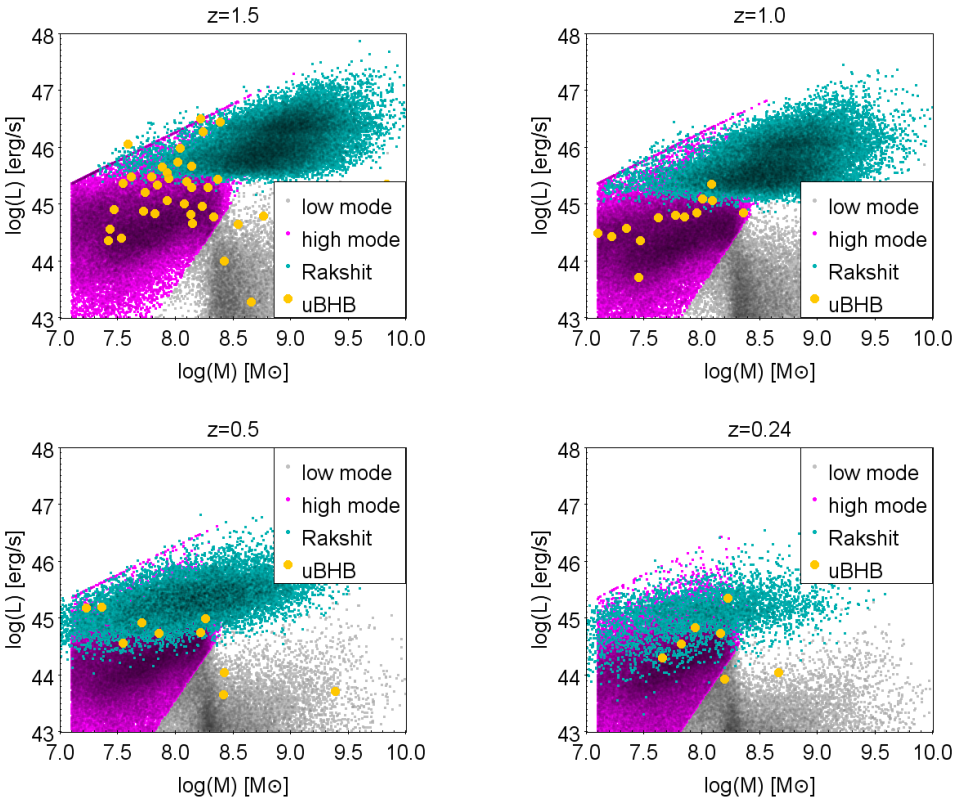

Figure 6: The mass to bolometric lumniosity of the Rakshit sample (blue) and high mode (pink), low mode (grey) and uBHB (yellow) populations of the simulation at the redshifts indicated at the top of the plot.

$]L_{min}, L_{max}[$ is therefore defined as

$$L_{min} = \bar{L}_{Rak} - \sigma_{L,Rak} \tag{26}$$

$$L_{max} = L_{Edd}. \tag{27}$$

With the mean bolometric luminosity $\bar{L}_{Rak}$ and its standard deviation $\sigma_{L,Rak}$ derived through a Gaussian curve fitted to the bolometric luminosity distribution of the Rakshit sample.

The matching mass range is on the lower side limited by either the Rakshit sample, which contains only the most massive AGN at higher redshifts, or the applied mass cut of BHs in the simulation. On the other side, the matching mass range is limited by the simulation because it does not produce massive BHs with high accretion rates (massive BHs switch to low accretion mode and are more likely to stay in that mode, see section 4.1.2). The matching mass range is therefore defined as the overlapping 2σ mass

ranges of the two populations:

$$M_{min} = max(\bar{M}_{Rak} - 2\sigma_{M,Rak}, 10^{7.1} M_{\odot}) \tag{28}$$

$$M_{max} = \bar{M}_{TNG,high} + 2\sigma_{TNG,high}. \tag{29}$$

With the mean mass $\bar{M}$ and its standard deviation σ derived through a Gaussian curve fitted to the respective mass distribution. Since the observations only overlap with BHs in high accretion mode of the simulation, only BHs in high accretion were considered. A 2σ interval is here sufficient to derive the matching range because the range is mainly limited by the Eddington luminosity on the lower side (especially at higher redshifts) and because the mass distribution of the simulation is not very well approximated by a Gaussian curve due to the two peaks (see Figure 3). In addition, with an 1σ interval the matching range would become smaller making it more susceptible to inaccuracies due to small sample sizes or even not possible to derive a binary fraction.

In table 5 the derived values for the matching mass and bolometric luminosity range can be seen.

z	M_{min} $[log(M_{\odot})]$	M_{max} $[log(M_{\odot})]$	L_{min} [erg/s]
1.5	8.1365	8.3966	45.7564
1.0	7.8438	8.3469	45.3898
0.5	7.1481	8.3068	44.9705
0.24	7.1	8.2811	44.6516

Table 5: The mass and bolometric luminosity range $]M_{min}, M_{max}[$ and $]L_{min}, L_{max}[$ in which the populations of simulation and observations match.

Through the mass and bolometric luminosity ranges, two matching populations of simulation and observations are derived. These matching populations are further compared in more detail. In figure 7 the mass distributions and in figure 8 the bolometric luminosity distributions of the matching populations can be seen. The population of the simulation is here scaled to the volume of the observations with the scalingfactor α.

The simulation shows way more BHs as observed in the matching range by a factor of ~ 100 (see figures 7 and 8). This is expected because the simulation is able to track all BHs, while observations are limited by other factors. Whether a source is detected and identified as an AGN depends on, for example, its orientation, the resolution of the observation, and the intergalactic medium. Besides, the distributions of the uBHBs (yellow) show only single peaks due to the scaling with α.

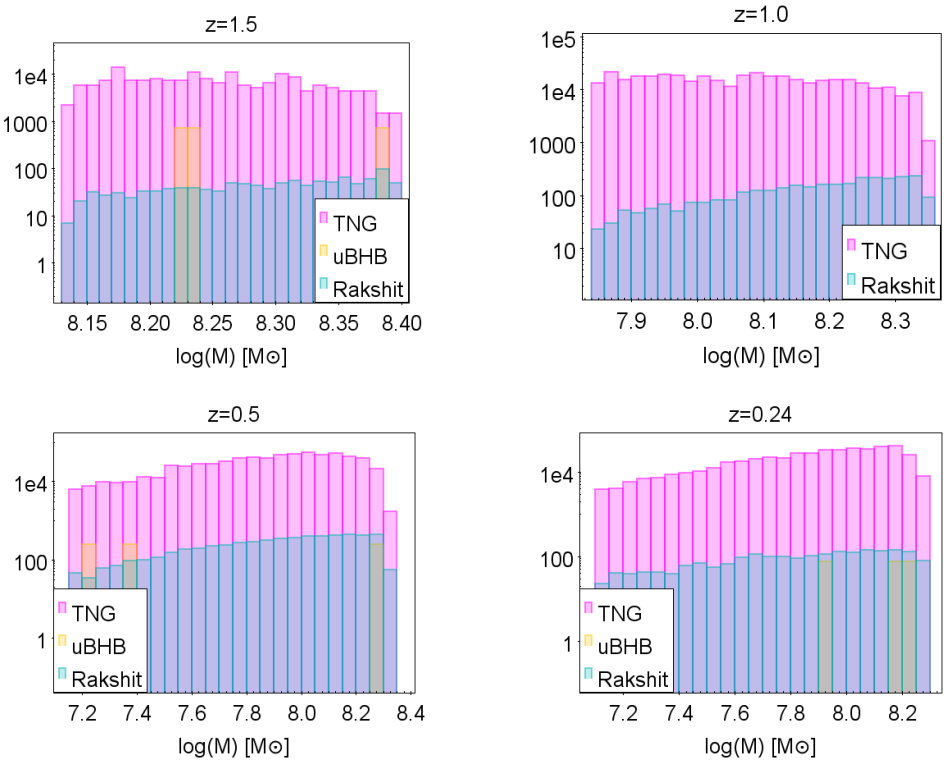

Figure 7: The mass distribution of simulation (pink) and the Rakshit sample (blue) in the mass and bolometric luminsoity range $]M_{min}, M_{max}[$ and $]L_{min}, L_{max}[$ at the redshift indicated on top of the plot. In yellow the uBHBs can be seen. At redshift $z = 1.0$ the simulation does not produce any uBHBs in that range.

Nevertheless, the distributions of the matching populations show, in general, a similar form. Just at the two lower redshifts, the bolometric luminosity distributions differ slightly at the low end and the very high end (see figure 8). This occurs due to the chosen 2σ interval of the matching mass range.

In conclusion, the simulation produces a BH population in a mass and bolometric luminosity range of $]M_{min}, M_{max}[$ and $]L_{min}, L_{max}[$ as observed by the SDSS surveys. The numbers of oBHs and uBHBs in the given ranges can be seen in table 6. A higher fraction of uBHBs in that range than the fraction derived in 4.1.5 is expected because uBHBs are likely to have a higher bolometric luminosity due to the assumption that their luminosity is the sum of the individual bolometric luminosities. Especially at the two higher redshifts the matching mass and bolometric luminosity ranges are relatively small. The relatively high fraction at z = 1.5 and the fraction of 0

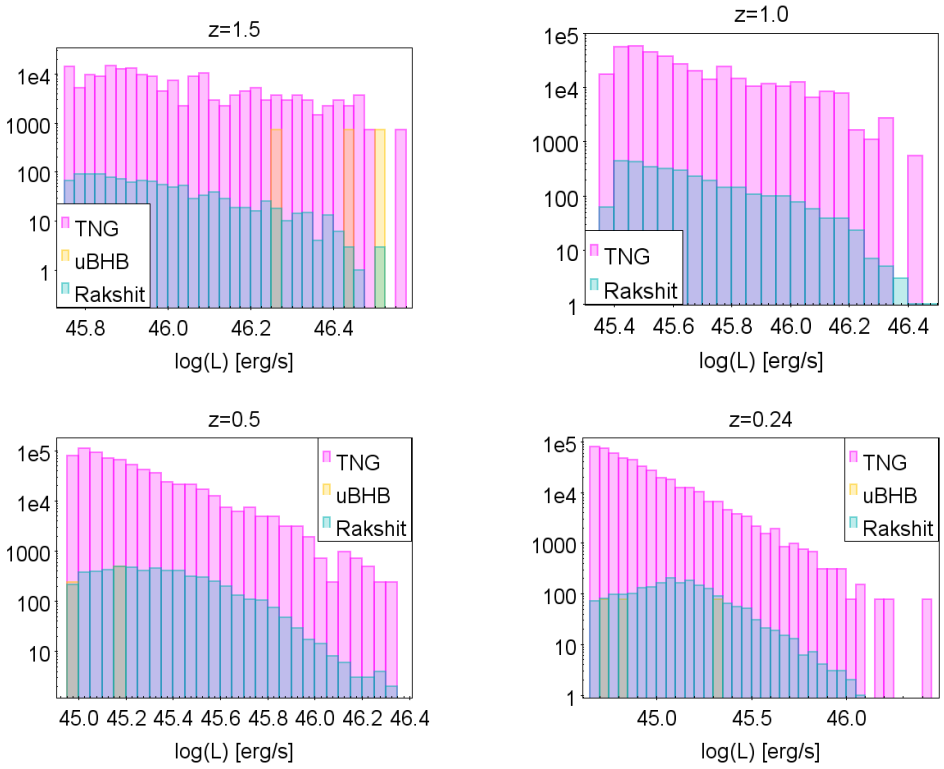

Figure 8: The luminosity distribution of simulation (pink) and the Rakshit sample (blue) in the mass and bolometric luminsoity range $]M_{min}, M_{max}[$ and $]L_{min}, L_{max}[$ at the redshift indicated on top of the plot. In yellow the uBHBs can be seen. At redshift $z = 1.0$ the simulation does not produce any uBHBs in that range.

at 1.0 are therefore believed to appear due to the small sample sizes of only 242 and 698 BHs at the respective redshifts.

z	# oBH	# uBHB	Fraction of uBHB [‰]
1.5	242	3	12.24
1.0	698	0	0
0.5	2859	3	1.05
0.24	6184	3	0.48

Table 6: Number of oBHs and uBHBs in the simulation with masses $M_{min} < M < M_{max}$ and bolometric luminosity $L_{min} < L_{bol} < L_{max}$. The populations of simulation and observations match sufficiently well in that ranges. uBHB coresponds to a binary system at a separation of $<$ 1arsec. The number of oBHs is the sum of all single BHs and uBHBs in the simulation. The fraction of uBHB is given by: $\#uBHB/\#oBH$.

5 Conclusion

The TNG300-1 run of the IllustrisTNG-model produces a BH population with broad distributions of mass and accretion rate. Only a small fraction are BHBs that would be unresolved in ground-based observations, meaning they have separations of $<$ 1arcsec (uBHBs). The BH population of the simulation coincides with the observed AGN population of the Rakshit sample in the mass and bolometric luminosity range given in table 5.

The derived fractions of uBHB in the simulation are shown in figure 9. In black, the uBHB fraction of all BHs in the simulation with masses $> 10^{7.1} M_{\odot}$ (see table 3). In red, the uBHB fraction of the BH population in the coinciding mass and bolometric luminosity range (see table 6). Both fractions decrease with time due to the increasing BH population and because the maximum observable separation of two BHs decreases, making it unlikely to find uBHBs in the simulation at lower redshifts.

Since the simulation reproduce a BH population as observed in the Rakshit sample in the given mass and bolometric luminosity range, the uBHB fraction of the simulation in that range can be applied to the Rakshit sample. Therefore, the simulation implies that in the observed AGN population of the Rakshit sample, at least 12.24‰in a redshift interval of $[1.4, 1.6]$, 0‰in $[0.9, 1.1]$, 1.05‰in $[0.4, 0.6]$ and 0.48‰in $[0.14, 0.34]$ are expected to host an unresolved BHB. The fractions of AGN hosting a BHB are lower limits due to the limited resolution of BHBs in the simulation (see section 4.1.4).

In table 7 the amount of observed AGN of the Rakshit sample in the coinciding mass and bolometric luminosity range at a given redshift interval can be seen. In addition, the minimal expected amount of AGN hosting a BHB derived using the fraction based on the simulation is shown.

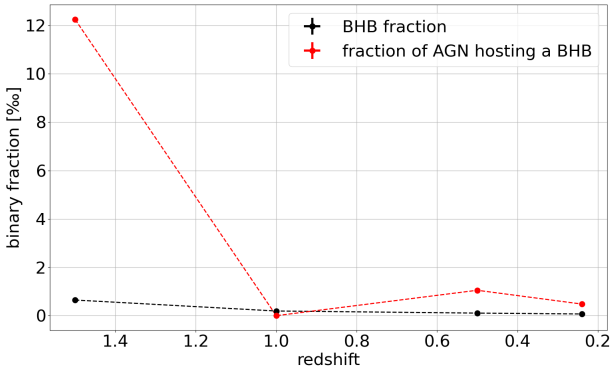

Figure 9: uBHB fractions of the simulation. It is differentiated between the uBHB fraction of all BHs with masses $> 10^{7.1} M_{\odot}$ (black, see table 3) and the uBHB fraction of the BH population that is similar in masses and bolometric luminosity to the AGN population of the Rakshit sample (red, see table 6).

z	# AGN	# AGN hosting a BHB
$1.4 - 1.6$	1134	14
$0.9 - 1.1$	3123	0
$0.4 - 0.6$	5627	6
$0.14 - 0.34$	2062	1

Table 7: Number of AGN and minimal expected amount of AGN hosting a BHB of the Rakshit sample in a mass and bolometric luminosity range as shown in table 5. The numbers were derived using the uBHB fraction of the simulation. The numbers are lower limits due to the limited resolution of the simulation.

6 Further research

This work suggests that a small fraction of AGN in the Rakshit catalog are powered by a black hole binary that is not resolved in ground-based observations. In figure 10 the total mass $M_{tot} = M_1 + M_2$ to separation s of the uBHBs in the simulation can be seen. The black line shows a mass to separation ratio that would produce gravitational waves with frequencies of $f_{GW} = 10^{-9}$Hz. The frequency f_{GW} is here estimated as the characteristic gravitational-wave frequency of a quasicircular black-hole binary, produced by the dominant (highest-order) quadrupole component, given by [49]:

$$f_{GW} = \left(\frac{M_{tot}}{s^3} \right)^{1/2} . \tag{30}$$

BHBs that appear above the black line in figure 10 produce gravitational waves with lower frequencies than f_{GW}. The lowest observable gravitational waves are observed with pulsar time arrays and have frequencies between $(10^{-9} - 10^{-7})$Hz [49].

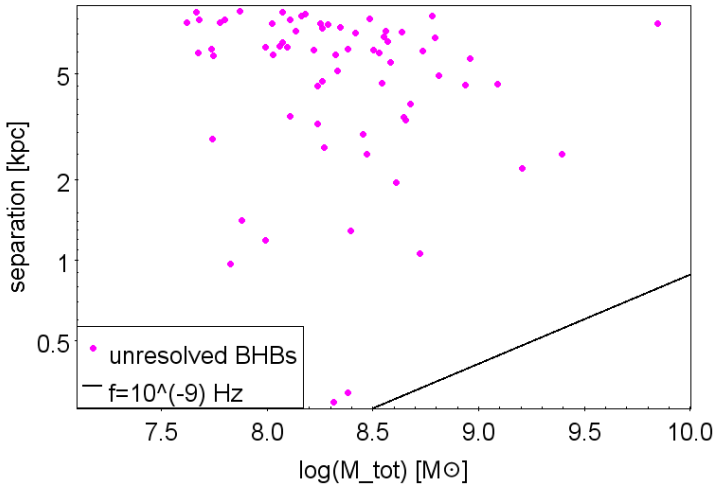

Figure 10: Total mass $M_{tot} = M_1 + M_2$ to separation of the uBHBs in the simulation. The black line shows a mass to separation ratio that would produce gravitational waves with frequencies of $f_{GW} = 10^{-9}$Hz.

As can be seen in figure 10 the uBHBs looked at in this work do not contribute to any observable gravitational waves at their current state. This is because the simulation has limited resolution for BHBs and already merges two BHs at separations where they do not emit gravitational waves with detectable frequencies. Nevertheless, all uBHB looked at in this work are merging before $z = 0$ and are therefore contributing to the gravitational wave background in the simulation in a further in spiral.

Furthermore, in the matching mass and luminosity range at $z = 1.5$, the TNG300-1 run contains 2 uBHBs where the distance s between the two BHs is $1 > s > 0.1$arcsec. For the respective redshifts $z = 1.0, 0.5, 0.24$ there are 0, 3 and 1 uBHBs with $1s > 0.1$arcsec. These binary systems would be resolved by space observations, which have a resolution of ~ 0.1arcsec. Therefore, it is expected that the Rakshit sample contains AGN that host a BHB, which could be resolved in future space observations. Applying the fraction of the simulation of uBHB with $s > 0.1$arcsec on the Rakshit sample shows that at least 9 and 6 BHBs in the center of an AGN at the redshift intervals $[1.4, 1.6]$ and $[0.4, 0.6]$ could be resolved. For redshifts $[0.9, 1.1]$ and $[0.14, 0.34]$ it results in zero expected AGN hosting a BHB. In addition, observations with higher resolution would not only be able to resolve AGN with binary systems, but also expand the observable BH population. With

a higher resolution, it is expected to find more lighter, not so luminous BHs. This could generally advance research in the field of galaxy evolution and BHs. In particular, it would be interesting for this work to see whether the simulation is able to recreate the BH population as it could be observed at lower luminosity or lower mass regions.

Also, the improvement of analytic methods and computing power can facilitate the development of new simulations with better resolutions. A large-scale simulation that also simulates BHBs until their coalescence would not only provide a more accurate estimation of AGN powered by a BHB, but also would have an impact on the current research on gravitational waves and the gravitational wave background.

References

[1] Simon White Houjun Mu, Frank van den Bosch. *Galaxy evolution and formation.* Cambridge University Press, 2010.

[2] R. F. Green M. Schmidt. Quasar evolution derived from the palomar bright quasar survey and other complete quasar surveys. *Astrophysical Journal, Vol. 269, p. 352-374*, 1983.

[3] Croom et. al. The 2df qso redshift survey - xii. the spectroscopic catalogue and luminosity function. *arXiv:astro-ph/0403040*, 2004.

[4] D. G. York et. al. The sloan digital sky survey: Technical summary. *arXiv:astro-ph/0006396*, 2000.

[5] M. Schmidt. 3c 273 : A star-like object with large red-shift. *Nature, Volume 197, Issue 4872, pp. 1040*, 1963.

[6] R. Bender G. Bower A. Dressler S. M. Faber A. V. Filippenko K. Gebhardt R. Green L. C. Ho J. Kormendy T. Lauer J. Magorrian S. Tremaine D. Richstone, E. A. Ajhar. Supermassive black holes and the evolution of galaxies. *arXiv:astro-ph/9810378*, 1998.

[7] M. Volonteri. *Formation of supermassive black holes.* The Astronomy and Astrophysics Review, 2010.

[8] R. Antonucci. Unified models for active galactic nuclei and quasars. *Annual Rev. Astron. Astrophys., Vol. 31, p. 473-521*, 1993.

[9] A.C. Fabian. Observational evidence of active galactic nuclei feedback. *Annual Review of Astronomy and Astrophysics Vol. 50: 455-489*, 2012.

[10] L. Hernquist T. Di Matteo, V. Springel. Energy input from quasars regulates the growth and activity of black holes and their host galaxies. *Nature, Volume 433, Issue 7026, pp. 604-607*, 2005.

[11] Magorrian et. al. The demography of massive dark objects in galaxy centers. *The Astronomical Journal, Volume 115, Issue 6, pp. 2285-2305*, 1998.

[12] D. Merritt L. Ferrarese. A fundamental relation between supermassive black holes and their host galaxies. *The Astrophysical Journal, Volume 539, Issue 1, pp. L9-L12*, 2000.

[13] Mark A. Hausman Jeremiah P. Ostriker. Cannibalism among the galaxies: Dynamical produced evolution of cluster luminosity functions. *The Astrophysical Journal, 217:L125-L129*, 1977.

[14] R. D.; Rees M. J. Begelman, M. C.; Blandford. Massive black hole binaries in active galactic nuclei. *Nature, Volume 287, Issue 5780, pp. 307-309*, 1980.

[15] David Merritt Miloš Milosavljević. Formation of galactic nuclei. *ApJ 563 34*, 2001.

[16] Ezequiel Treister Sylvain Veilleux Ranjan Vasudevan Margaret Trippe Michael Koss, Richard Mushotzky. Understanding dual active galactic nucleus activation in the nearby universe. *ApJL 746 L22*, 2012.

[17] Yue Shen Xin Liu Nadia L. Zakamska Qian Yang Jennifer I. Li u Ching Chen, Hsiang-Chih Hwang. Varstrometry for off-nucleus and dual subkiloparsec agn (vodka): Hubble space telescope discovers double quasars. *ApJ 925 162*, 2022.

[18] B. P. Abbott et al. Observation of gravitational waves from a binary black hole merger. *Phys. Rev. Lett. 116, 061102*, 2016.

[19] Zaven Arzoumanian et al. The NANOGrav 12.5 yr data set: Search for an isotropic stochastic gravitational-wave background. *ApJL 905 L34*, 2020.

[20] The NANOGrav Collaboration. The NANOGrav 15-year data set: Constraints on supermassive black hole binaries from the gravitational wave background. *arXiv:2306.16220v2*, 2023.

[21] C. Rodriguez et. al. A compact supermassive binary black hole system. *ApJ 646 49*, 2006.

[22] Schaye et. al. The EAGLE project: simulating the evolution and assembly of galaxies and their environments. *Monthly Notices of the Royal Astronomical Society, Volume 446, Issue 1, p.521-554*, 2015.

[23] Vogelsberger et. al. The illustris simulation: the evolving population of black holes across cosmic time. *Monthly Notices of the Royal Astronomical Society, Volume 452, Issue 1, p.575-596*, 2015.

[24] Dylan Nelson Shy Genel Jill Naiman Rudiger Pakmor Lars Hernquist Paul Torrey Mark Vogelsberger Rainer Weinberger Federico Marinacci Annalisa Pillepich1, Volker Springel. Simulating galaxy formation with the illustristng model. *arXiv:1703.02970v2*, 2017.

[25] Dubois et. al. Self-regulated growth of supermassive black holes by a dual jet–heating active galactic nucleus feedback mechanism: methods, tests and implications for cosmological simulations. *Monthly Notices of the Royal Astronomical Society, Volume 420, Issue 3, March 2012, Pages 2662–2683*, 2012.

[26] Rainer Weinberger. Simulating galaxy formation with black hole driven thermal and kinetic feedback. *arXiv:1607.03486v2*, 2017.

[27] Suvendu Rakshit. Spectral properties of quasars from sloan digital sky survey data release 14: The catalog. *The Astrophysical Journal Supplement Series, 249:17 (24pp)*, 2020.

[28] David W. Hogg. Distance measures in cosmology. *arXiv:astro-ph*, 2000.

[29] Planck Collaboration. Planck 2015 results. xiii. cosmological parameters. *AA, 594, A18*, 2016.

[30] P. J. E. Peebles. *Principles of Physical Cosmology.* Princeton: Princeton University Press, 1993.

[31] E. L. Wright. A cosmology calculator for the world wide web. *arXiv:astro-ph*, 2018.

[32] Jeremiah P. Ostriker Thorsten Naasb. Theoretical challenges in galaxy formation. *Annu. Rev. Astron. Astrophys. 2017. 55:59–109*, 2017.

[33] Simon D. M. White G. De Lucia C. S. Frenk L. Gao A. Jenkins G. Kauffmann J. F. Navarro N. Yoshida Darren J. Croton, Volker Springel. The many lives of active galactic nuclei: cooling flows, black holes and the luminosities and colours of galaxies. *Monthly Notices of the Royal Astronomical Society, Volume 365, Issue 1, Pages 11–28*, 2006.

[34] Monica Colpi Marta Volonteri, Melanie Habouzit. The origin of massive black holes. *Nature Reviews Physics*, 2021.

[35] S. D. M. White M. J. Rees. Core condensation in heavy halos: a two-stage theory for galaxy formation and clustering. *Monthly Notices of the Royal Astronomical Society, Vol. 183, 341-358*, 1978.

[36] R. Wielebinski E. M. Berkhuijsen. Structure and properties of nearby galaxies. *D. Reidel Publishing Company*, 1978.

[37] B. Paczynski. Thick accretion disks around black holes. *Mitteilungen der Astronomischen Gesellschaft Hamburg 57, 27*, 1982.

[38] Richard Edgar. A review of bondi–hoyle-lyttleton accretion. *arXiv:astro-ph*, 2004.

[39] T.; Ballantyne D. R.; Bonetti M. Li, K.; Bogdanović. Massive black hole binaries from the tng50-3 simulation. i. coalescence and lisa detection rates. *ApJ 933 104*, 2022.

[40] S. Chandrasekhar. Dynamical friction. i. general considerations: the coefficient of dynamical friction. *Astrophysical Journal, vol. 97, p.255*, 1943.

[41] David Merritt Miloš Milosavljevic. The final parsec problem. *arXiv:astro-ph/0212270v2*, 2003.

[42] D. Merritt E. Vasiliev, F. Antonini. The final-parsec problem in the collisionless limit. *ApJ 810 49*, 2015.

[43] Megan C. Urry Jong-Hak Woo. Active galactic nucleus black hole masses and bolometric luminosities. *The Astrophysical Journal, Volume 579, Issue 2, pp. 530-544*, 2002.

[44] Paul Torrey Ewald Puchwein Mark Vogelsberger, Federico Marinacci. Cosmological simulations of galaxy formation. *arXiv:astro-ph*, 2019.

[45] The TNG Collaboration. IllustrisTNG - project description, 2023. https://www.tng-project.org/about/ Accessed on 20.12.2023.

[46] Volker Springel. Galiliean-invariant cosmological hydrodynamical simulations on a moving mesh. *arXiv:0901.4107v3*, 2010.

[47] Marta Volonteri. Formation of supermassive black holes. *The Astronomy and Astrophysics Review, Volume 18, Issue 3, pp.279-315*, 2010.

[48] The TNG Collaboration. TNG300-1 configurations, 2023. https://www.tng-project.org/data/downloads/TNG300-1/ Accessed on 01.10.2023.

[49] James R. van Meter Joan Centrella, John G. Baker. Black-hole binaries, gravitational waves, and numerical relativity. *arXiv:1010.5260v2*, 2010.

Acknowledgements

This work and the accompanying experiences would not have been possible without the help of many people. I would therefore like to thank these people for their help and support.

First of all, Professor José Afonso and his research group, who warmly welcomed me into their research group at the observatory in Lisbon. Here I had the opportunity to gain my first insights into the day-to-day work of an astrophysicist and learn about the interesting history of the universe. In addition, José Afonso in particular was always on hand to answer my questions and was always able to help me with his patient and structured explanations. He also helped me after my stay in Lisbon to put my work on paper and structure it, for which I am very grateful.

I would also like to thank Professor Kai Schmitz. He was the professor in charge at my university in münster. Thanks to him, I had someone at my side who looked at my work from a more theoretical point of view. He also brought the aspect of gravitational waves and binary systems into my work. Thanks to the collaboration between José Afonso and Kai Schmitz, we were able to find the highly exciting topic that combines aspects of the research fields of both of them.

Thanks also to my friends and family, with whom I have always felt connected despite the great distance. They gave me the support and courage to make the decision to go to Lisbon.

A Quality flags in the Rakshit catalog

The Rakshit catalog provides quality flags for certain properties. In table 8 the criteria can bee seen that is used to calculate the quality flag of the continuum luminosity and emission lines as $2^{Bit_0} + 2^{Bit_1} + 2^{Bit_2} + ... + 2^{Bit_n}$. If a criterion is fulfilled, the respective bit is set to 1, otherwise to 0.

The quality flag of the bolometric luminosity corresponds to the quality flag of continuum luminosity. The quality flag of mass is calculated as the sum of the quality flags of continuum luminosity and emission lines.

Bits	continuum luminosity	emission lines
Bit_0	luminosity or its uncertainty is zero or NaN	relative uncertainty of peak flux >1/3
Bit_1	relative uncertainty of luminosity >1.5	luminosity or its uncertainty is zero or NaN
Bit_2	slope or its uncertainty is zero or NaN	relative uncertainty of luminosity >1.5
Bit_3	slope hits a limit in the fit	FWHM or its uncertainty is zero or NaN
Bit_4	reduced χ^2 of the continuum fit > 50	FWHM < 910km/s
Bit_5	0	relative uncertainty of FWHM >2
Bit_6	0	velocity offset or its uncertainty is zero or NaN
Bit_7	0	velocity offset value hits lower or upper limit in the fit
Bit_8	0	uncertainty in velocity offset >1000 km/s

Table 8: Criteria used to calculate quality flags of continuum luminosity and emission lines in the Rakshit catalog. The Quality flags are used to qualify properties such as BH mass and accretion rate [27].

Declaration of Academic Integrity

I hereby confirm that this thesis, entitled Estimating the fraction of Active Galactic Nuclei hosting a black-hole binary with cosmological simulations is solely my own work and that I have used no sources or aids other than the ones stated. All passages in my thesis for which other sources, including electronic media, have been used, be it direct quotes or content references, have been acknowledged as such and the sources cited. I am aware that plagiarism is considered an act of deception which can result in sanction in accordance with the examination regulations.

22.12.2023, Peer Wuttke

(date, signature of student)

I consent to having my thesis cross-checked with other texts to identify possible similarities and to having it stored in a database for this purpose.

I confirm that I have not submitted the following thesis in part or whole as an examination paper before.

22.12.2023, Peer Wuttke

(date, signature of student)